Effect of Fiber-Form Nanostructure on the Particle Emissions from Tungsten Surface in Plasmas

Shuichi TAKAMURA†, Takanori MIYAMOTO†, Noriyasu OHNO††

Abstract The effects of fiber-form nanostructure of tungsten surface on both the electron emission and the sputtering in helium/argon plasmas are represented. Generally nano-fiber forest made of tungsten with helium gas inside was found to have a tendency of suppressing the particle emission. The electron emission comes from the impact of high energy primary electrons. In addition, a deeply biased tungsten target which inhibits the influx of even energetic primary electrons seems to produce an electron emission, and it may be suppressed on the way to nanostructure formation on the surface of W target. Such an emission process is discussed here. The sputtering yield of He-damaged tungsten surface with the fiber-form nanostructure depends on the surface morphology while the sputtering itself changes the surface morphology, so that the time evolutions of sputtering yield from the W surface with originally well-developed nanostructure was found to show a minimum in sputtering yield. The surface morphology at that time is for the first time made clear with FE-SEM observation. The physical mechanism for the appearance of such a minimum in sputtering yield is discussed.

1. Introduction

In ITER and DEMO Reactor, Tungsten materials are focused for the plasma-facing component. However, the fiber-form nanostructure containing helium bubbles on the tungsten (W) surface [1～3] generated by the irradiation of He, one of the fusion reaction products, has been worried, due to an apparent weakness against the heat load [4] and easy triggering of unipolar arcing [5, 6]. On the other hand, various kinds of surface characteristics, apparently favorable for fusion, have been found, for example, an increase in surface cooling capability [7, 8], a suppression of electron emission leading to an reduction in power transmission factor through the sheath in front of the tungsten surface [8], also a suppression of physical sputtering [9, 10] due to heavy ions, like argon and neon, which will be introduced into SOL for the plasma cooling there as radiators, and some resistance against cracking due to thermal shocks [11].

†　愛知工業大学　工学部　電気学科（豊田市）
††　名古屋大学　工学研究科（名古屋市）

In this research work, new findings concerning the effects of W forest made of very thin fibers with bubbles inside on the particle emissions from such a complex surface are summarized.

The nano-fiber jungle was found to play a role of suppressing the secondary electron emission (SEE) due to impinging primary energetic electrons, which also contribute to surface cooling through a reduction in power transmission factor [12]. SEE has a great influence on the electronic power flux to the plasma-facing surface exposed by a transient heat load, like ELM [13]. It has been surprisingly found that the deeply negatively biased target to which energetic electrons produced in this device may not arrive has also a generation and/or a suppression of electron emission from W target. The mechanism is discussed in this paper.

The sputtering yield of He-damaged tungsten surface with the fiber-form nanostructure was found to depend on the surface morphology. A well-developed blackened tungsten surface has a substantially small sputtering yield compared with the flat non-damaged surface. Then, a sputtering minimum is obtained after some advancement of sputtering by

heavy particles like argon. The surface morphology at that time is quite different from the virgin nanostructure. The physical process to have a sputtering minimum is needed to be discussed.

In the next section, we will introduce you the compact plasma device and measuring technique. The phenomena related to electron emissions including SEE are discussed in the following section. Section 4 is devoted to the physical sputtering processes, and finally the summary and conclusion will be given.

2. Experimental procedure

The linear plasma device for the present study is called AIT-PID (Aichi Institute of Technology-Plasma Irradiation Device) in which the radial confinement of high density plasma is obtained by a multicusp magnetic configuration. Three pairs of neodymium permanent magnet bars are employed and produces a weak magnetic zone in the central axis region of chamber. In addition a solenoidal winding underneath the magnets produces a weak axial magnetic field up to 10mT [14]. In this device, the high density helium plasmas contain hot electron component. The bulk electron temperature T_{ec} is about 4eV, while the hot electron component with the fraction of roughly 8% has an apparent temperature of up to 40eV. But the energy distribution of hot electrons is not a complete Maxwellian but has a cut at around the discharge voltage of about 100eV. Figure 1 shows a typical probe characteristics, where (a) represents a logarithmic plot of electronic current as a function of probe voltage with respect to the grounded chamber, and the current becomes extremely small compared with a Maxwellian for the tail distribution beyond about 60 eV. The proper analysis of voltage-current relation is shown in Fig. 1(b), focusing on the separation of cold electron population from the hot one. First we determine the hot electron temperature from the slope of tail distribution and the density from its saturation current corresponding to the current at the plasma potential and then subtract the current corresponding to the hot component from the total one. Then we obtain the current coming from the cold electrons, giving its temperature and its density.

Therefore, we can determine the hot component fraction $\alpha = n_{eh}/(n_{ec} + n_{eh})$ and the temperature ratio β defined by T_{eh}/T_{ec}, where "h" and "c" in the subscript mean the hot and bulk electron component, respectively.

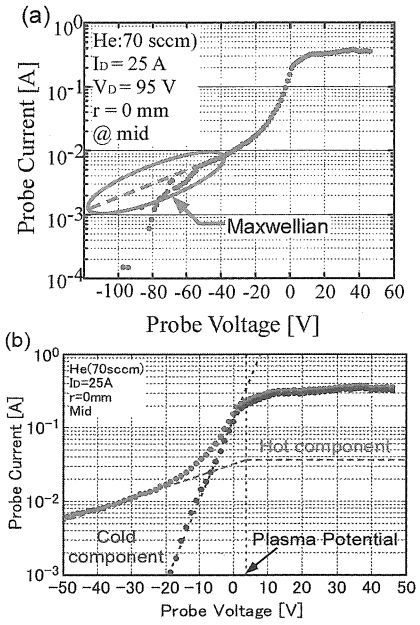

Figure 1. Langmuir probe characteristics and its analysis. (a) shows a cut of electron energy distribution at more than about 60 eV, showing an incomplete Maxwellian. (b) indicates a procedure to obtain firstly the hot electron temperature from the slope of tail and its density from the corresponding electron saturation current. Then the subtraction of hot electron contribution to the electron current from the total electron current gives the bulk electron temperature and density.

Figure 2 shows the fiber-form nanostructure on the tungsten surface made in AIT-PID where we have high density ($\sim 10^{18}$ m^{-3}) helium plasmas with the ion bombarding energy of 50eV and the starting surface temperature of 1420K measured with IR-thermometer which employs the infrared line of 0.9 μm, corresponding to the spectral emissivity for non-damaged tungsten of 0.42～0.43 at that range of surface temperature. The helium ion fluence is $\sim 10^{26}$ m^{-2}. The specimen is a cold worked powder metallurgy tungsten (PM-W) fabricated by compressing the tungsten powder and sintered in a reduced atmospheric pressure.

Another method for tungsten temperature measurement is provided because the modified surface due to He defects may have a completely different spectral emissivity from that of the flat non damaged tungsten surface. R-type (platinum x platinum–rhodium (10%)) thermocouple with an insulated sheath structure makes a direct measurement of tungsten temperature on the way to blackening as well as the floating potential in He plasmas. The sheath diameter of thermocouple is as thin as 0.5 mm.

In order to detect the tungsten atomic spectra, a spectrometer (Ocean Optics Inc., HR-4000) has been used with fiber optics through a quartz vacuum window. An interference optical filter focusing on WI atomic line (498.26nm) was also used to obtain the sputtering pattern of tungsten atoms in argon

as well as helium plasmas

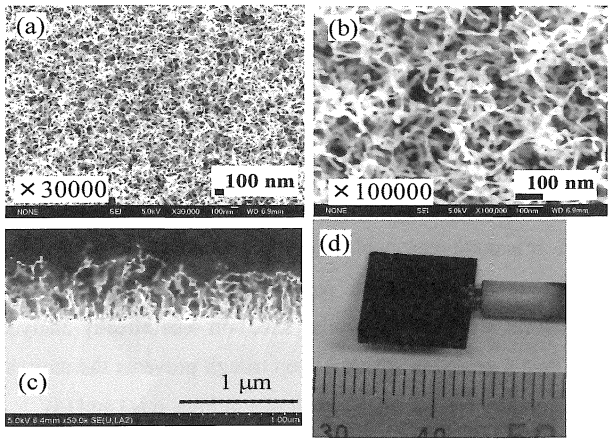

Figure 2. Fiber-form nanostructure of PM-W tungsten with a complete black color obtained by He exposure in AIT-PID. (a) and (b) show top surfaces with different SEM magnifications, (c) does its cross-section, and (d) is the photo showing a surface blackening.

3. Suppression of electron emission

3.1. Secondary electron emission

The two electron temperature helium plasma gives a deep floating potential of around -40V with respect to the vacuum chamber. Considering the plasma potential of +4 ~ 5V, the sheath voltage of 45V is very high compared with the normal sheath voltage $\sim 4T_{ec} = 16$V without taking hot component into account. Such a high sheath voltage may be explained by the numerical analysis [8] on the floating condition that the primary electron flux composing of bulk and tail component balances with the ion one although the value of 45V is rather smaller than the numerical prediction assuming a complete Maxwellian distribution even for hot electrons. The floating condition is obtained by equating the ion saturation current with the electron current composed of two components:

$$\left(1-\alpha+\frac{\alpha}{\beta}\right)^{-1/2} = \sqrt{\frac{m_i}{2\pi m_e}}\left\{(1-\alpha)e^{e\phi_f/T_{ec}} + \alpha\sqrt{\beta}e^{e\phi_f/T_{eh}}\right\} \qquad (1)$$

where the secondary electron emission is not considered, m_e and m_i are the electron and ion masses, respectively. The left-hand side corresponds to the ion saturation current. Fig. 3 shows the normalized floating potential $e\phi_f/T_{ec}$ as a function of the temperature ratio β, taking the hot electron fraction α as a parameter. When β = 40/4 = 10, and α = 0.08 (8%), then $e\phi_f/T_{ec}$= -20, meaning $\phi_f = -20 \cdot T_{ec}$ = -80 ~ -100 eV, while the starting sheath voltage is ~-50 V.

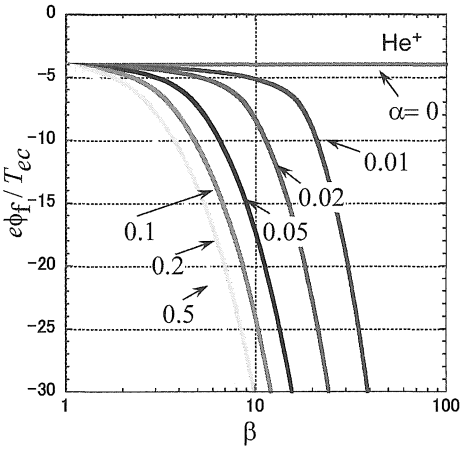

Figure 3. The normalized sheath voltage $e\phi_f/T_{ec}$ as a function of the temperature ratio β, taking the hot electron component fraction as a parameter.

Figure 4 shows the time evolutions of the floating potential and the tungsten temperature observed with the IR-thermometer as well as the thermocouple on the way to nanostructure formation. The tungsten target has a dimension of $15\times15\times1$ mm^3 with a hole of 0.5 mm in diameter for the insertion of thermocouple, which is parallel to the tungsten surface. The drop of tungsten temperature down to more than 300K demonstrates a clear cooling. The floating potential changes rapidly from -38 down to deeper than -50V during the period of large change in tungsten temperature, meaning a clear correlation with nanostructure formation on the surface.

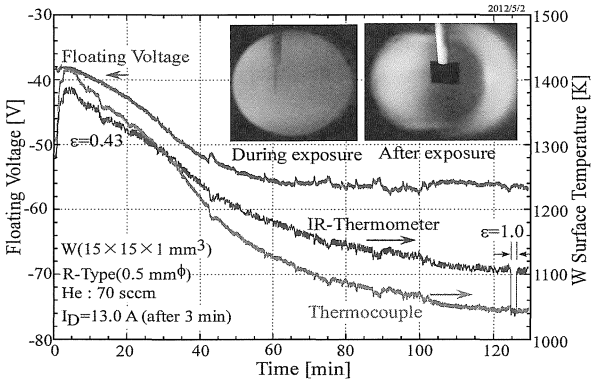

Figure 4. Temporal evolutions of surface temperatures measured with R-type thin thermocouple as well as IR-thermometer, and the floating potential of W target ($15\times15\times1$ mm^3) on the way to nanostructure formation.

Figure 5 shows an alternative representation for deepening of floating potential on the way to nanostructure formation by observing the temporal evolution of biasing current when the biasing voltage is fixed at -50V. At first the biasing current is

negative, meaning an ionic current due to the floating potential shallower than -50V, and at about 30 min later the biasing current crosses zero, corresponding that the floating potential just equals to the biasing one, then moving to the area where the electronic biasing current flows, that is the floating potential becomes deeper than -50V, finally it arrives at -60V.

The insertion of Fig. 5 shows a schematic dependence of power transmissions factor through the sheath on the sheath potential. At the beginning the biasing from the floating (～40V) to -50V brings a decrease in tungsten temperature, and the biasing from -50V to the floating (～60V) does again another decrease in the temperature at the final stage. These behaviors can be well explained by using the insertion diagram. Therefore, we can say that the deepening in the floating potential as observed in Fig. 4 contributes somewhat to the surface cooling due to the reduction in the plasma heat load through the sheath. However, a substantial temperature drop has been observed even at a fixed biasing voltage as shown in Fig. 5. This comes from an increase in total emissivity, resulting in an enhanced thermal radiation loss.

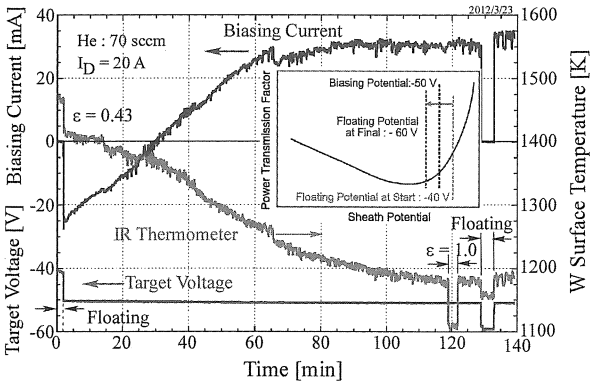

Figure 5. Time traces of the biasing current, the temperature obtained by IR-thermometer and the target biasing voltage on the way to blackening of tungsten target (10×10×0.035 mm^3). The insertion shows a schematic diagram for the sheath potential dependence of power transmission factor, where -50V correspond to the biasing potential, -40V does the floating potential at the start in He plasma exposure, and -60V that at the final stage.

Tungsten has a fairly high SEE coefficient. The Maxwellian electrons with the temperature of 40eV give almost 1.0 for the SEE yield [15] as shown in Figs. 6 (a) and (b). Therefore, the floating potential for the normal flat tungsten surface seems to be influenced by the electron emission in the presence of hot electrons in He plasma. The electron emission makes the floating potential of W target shallow at the initial stage of He plasma irradiation. If we do not consider hot electron component, we obtain the following expression for the floating potential for mono-Maxwellian electron plasma,

$$e\phi_f = T_e \ln\left\{ M\sqrt{\frac{2\pi m_e}{m_i}} + \frac{j_{em}^-}{(en_{se}/4)\sqrt{8T_e/\pi m_e}} \right\}, \qquad (2)$$

where T_e is the electron temperature in energy unit, n_{se} is the plasma density at the sheath edge, and j_{em}^- is the electron emission current density.

Deepening of floating potential on the way to nanostructure formation has been thought to come from the reduction in SEE yield. It is quite reasonable since the secondary electrons cannot come out to the sheath region through a forest of nano fiber-form structure. A similar situation was already analyzed by Ohya's group, in which a deep trough prevents the emission of secondary electrons [16] as shown in Figs. 6 (c) and (d).

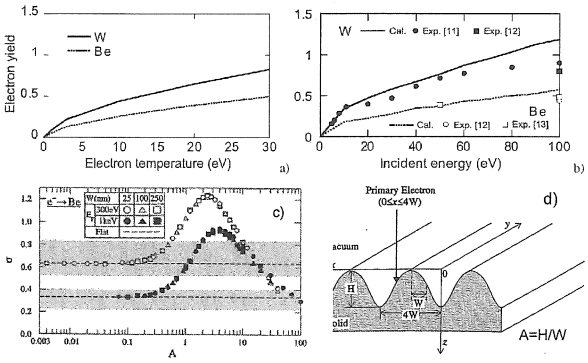

Figure 6. SEE from tungsten surface. SEE yields as a function of electron temperature (a) and electron energy (b) [15]. The effect of surface angulation on SEE is shown in (c). The aspect ratio A is defined by the ratio of H to W asshown in (d). A deep trough prevents the emission of secondary electrons [16].

3.2. Ion induced electron emission

It has been found that a deep biasing of W target in He plasmas, producing fiber-form nanostructure quickly, also bring some reduction in the ionic biasing current as shown in Figs. 7 and 8, where the biasing voltage is -95 and down to -240V, respectively. Here, the energetic electrons play no role since they cannot arrive at the target coming over such a high potential barrier. The nanostructure formation may expand a little bit its effective surface area although the thickness of plasma sheath is much larger than the typical scale of nanostructure, at most a few micrometers. If we can assume that the electron emission due to He ion incidence would be suppressed by the development of fiber-form nanostructure, then the time evolution of ionic biasing current may be explained. Then, we have to recognize the importance of ion induced electron emission. It comes either Auger electron emission [17～18] or ion bombarding SEE [19]. Schematic energy-level diagram for the ion-metal system, illustrating

Auger neutralization of the ion is shown in Fig. 9. One electron from the conduction band of the metal neutralizes the ion near the surface. The energy released by the first electron is absorbed by a second electron from the metal. If the energy transferred to this second electron is large enough and its momentum properly oriented, this electron can escape from the metal.

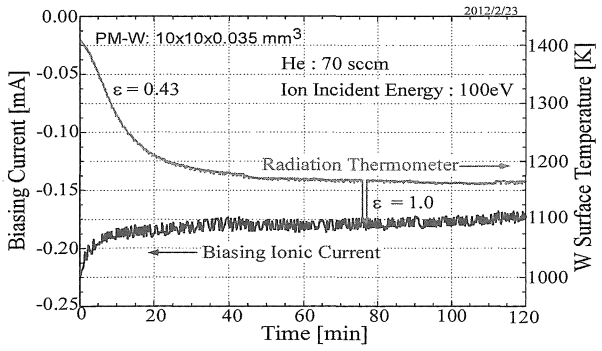

Figure 7. Reduction in ionic biasing current on the way to blackening for a deep biasing voltage, -95V.

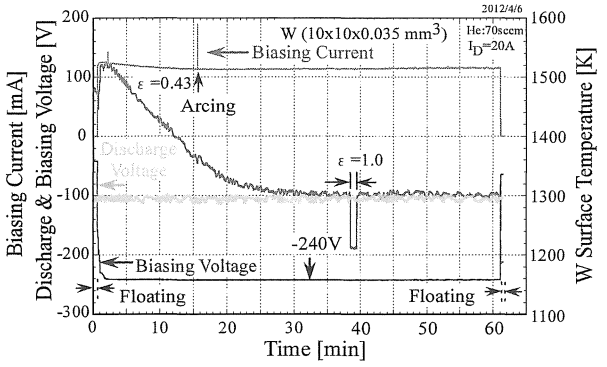

Figure 8. Reduction in ionic biasing current on the way to blackening for a very deep biasing voltage, -240V. Arcing is detected at 15 min after the exposure start. The trace of discharge voltage is a measure of discharge stability.

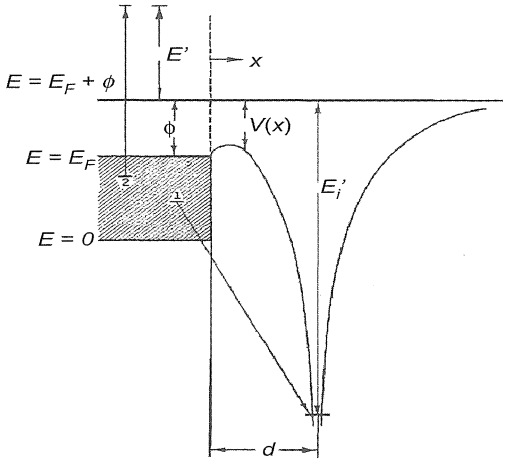

Figure 9. Energy diagram of metal surface and incident noble gas ion system, illustrating Auger neutralization of the ion[17~19].

From this observation, we have to confirm SEE due to energetic electrons independently of ion induced effect and its suppression owing to the nanostructure formation. In order to avoid the ionic incidence on the target, the biasing potential for the blackened tungsten was raised up to +6V more than the plasma potential. The process is now shown in Fig. 10, incidentally temporal increase in surface temperature is observed after arriving at 1700K apparently with use of IR-thermometer. This comes from a reduction in total emissivity because the nanostructure is shrinked, and the surface becomes flattened [7], and finally restores the original flat surface [20, 21] which we call a "recovery". The recovery restores the SEE, making a reduction in biasing electronic current.

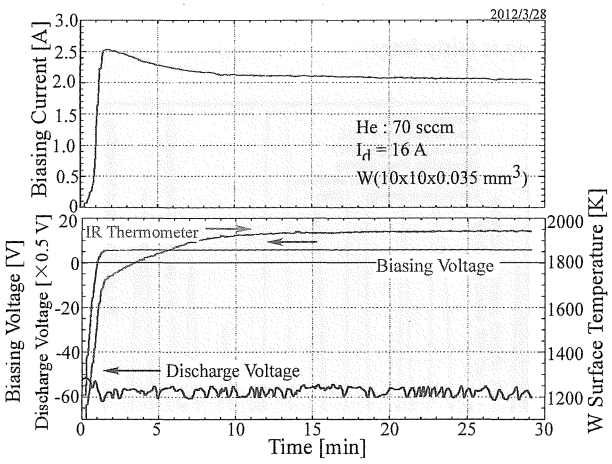

Fig.10 Recovery process with plasma electron annealing. Reduction in biasing electron current on the way to recovery of tungsten surface from blackened one to normal flat one. The biasing voltage of +6V is higher than the plasma potential, inhibiting the ion incidence to the target.

Another confirmation is to check the time evolution of ion biasing current when the nanostructure is broken progressively by Ar physical sputtering. It is represented in Fig. 11 where an increase in the ion biasing current is clearly shown as expected.

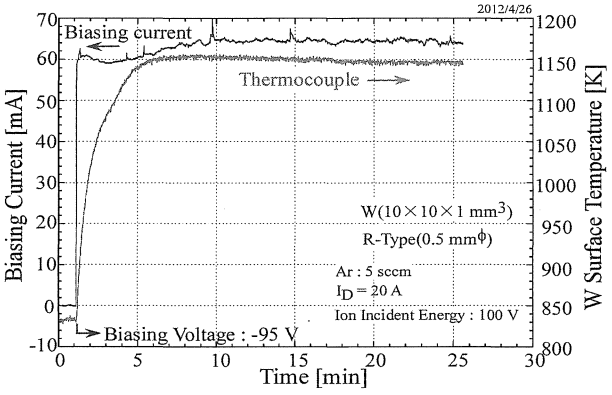

Figure 11. Surface recovery with Ar ion sputtering. The negative biasing enhances the physical sputtering which breaks the fiber-form nanostructure. The ion biasing current was observed to increase a little bit according to the annihilation of nanostructure. The nanostructure is considered to inhibit the ion-induced electron emission.

4. Suppression of atomic emission

The effects of fiber-form nanostructure on the physical sputtering by heavy particles like argon have been investigated [9,10]. The most impressive phenomenon is a substantial suppression of sputtering yield. In more detail, the time evolution of tungsten atomic line emission shows a minimum after several minutes from the start of sputtering. In the present case, tungsten atomic spectral lines are first sought for the detection of atomic emission in argon plasmas, as is shown in Fig. 12 where the thick line shows a spectrum with sputtering and the thin line does one without sputtering. From the ratio of spectral line intensities w and w/o sputtering, WI(498.26nm) was chosen for the measure of sputtering yield [22], because the above ratio is fairly large.

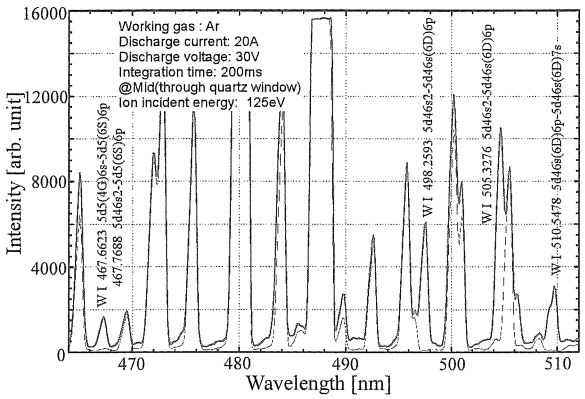

Figure 12. Visible light spectra of Ar plasma w and w/o sputtering from tungsten target.

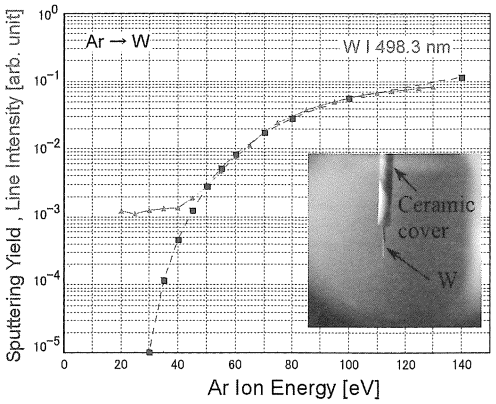

Figure 13. Comparison between sputtering yield of tungsten by Ar bombardment and spectral intensity WI (498.3nm) as a function of Ar incident energy.

The squares in Fig. 13 shows the curve for W sputtering yield as a function of Ar ion incident energy, obtained from NIFS (National Institute of Fusion Science) data base. The triangle shows the intensity of WI(498.26nm) as a measure of sputtering yield. The intensity at 100eV is made to coincide with the sputtering yield. The Ar ion energy dependence of the WI intensity fits well with the sputtering yield over the range between 50 and 130 eV so that WI intensity is considered to be a good measure of physical sputtering yield.

We observed the special patterns of tungsten atomic line by taking photos through the interference filter for 498.26nm (Andover Co.; FWHM: 1.0 ± 0.2nm, 3 cavities, 50 mm in diameter). Figure 14 represents two patterns of W atoms in Ar and He plasmas. The sputtering yield by Ar ion is much larger than by He ion. Clear image is obtained as shown in Fig.14(a) with the ion incident energy of 105eV, while the image for He^+ is very weak even for the incident energy of 255eV since the sputtering yield of W by He is much smaller than that by Ar. The W sputtering yield of 2×10^{-2} is obtained for Ar^+ of 60eV and for He^+ of 400eV. The spatial asymmetry in line emission distribution comes from the location of cathode for the plasma production. In this case it is located left hand side. The axial profile of WI intensity shows some decay whose typical length is determined by the electron impact ionization of sputtered tungsten atoms for a few eVs in kinetic energy in plasmas.

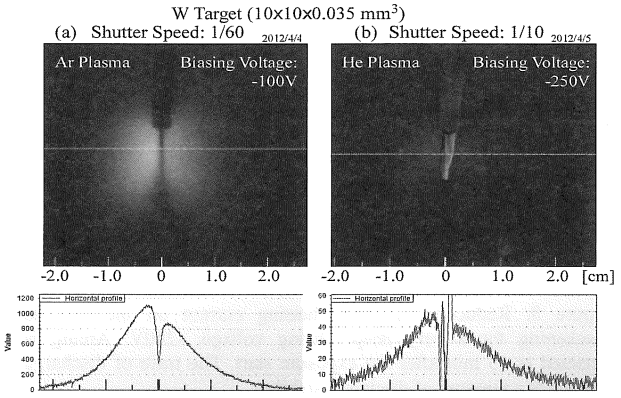

Figure 14. Sputtering patterns of tungsten due to Ar ion bombardment and He ion one. The top figure shows photos taken through the interference filter while the bottom 1-D profiles along the line shown in the top, perpendicular to the target, corresponding to the line parallel to the axis of vacuum chamber.

The time history of WI intensity for the originally blackened W with fiber-form nanostructure is shown in Fig. 15 with a fixed biasing voltage. We note that the sputtering yield shows a minimum after 1 min later, and becomes a half of the starting value, then gradually increases, and finally shows a saturation corresponding to that of the flat normal tungsten. The minimum sputtering is about 1/5 of the normal value in the present case. The comparison of the surface morphologies between virgin blackened tungsten with thin fiber-form nanostructure on its surface and that showing a minimum sputtering yield is very curious and is shown in Fig. 16 where (a) and (b) are the cross

section and the top surface of original nanostructure and (c) and (d) corresponds to those for the surface morphology at the sputter minimum. The magnification is a half of virgin blackened tungsten. The fiber diameter is roughly 4 times thicker than the original fiber, probably due to the growth caused by the attachment of sputtered tungsten atoms. When such a growth proceed, the surface area facing to the incident Ar ions becomes large compared with the surface occupied by deep troughs or valleys. The relative surface areas of ion facing tungsten and the deep troughs or valley determines the sputtering yield. Anyway the fiber-form nanostructure plays a role of sputtering suppression.

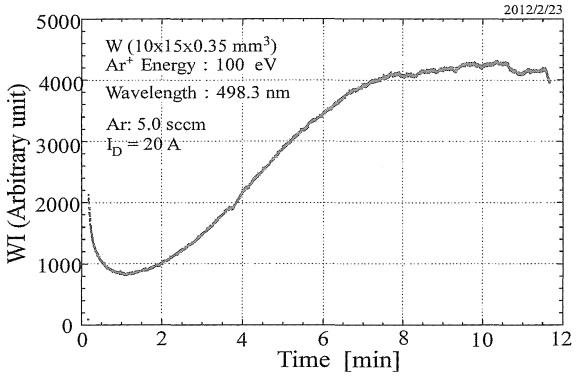

Figure 15. Time evolution of WI spectral line corresponding to sputtering yield

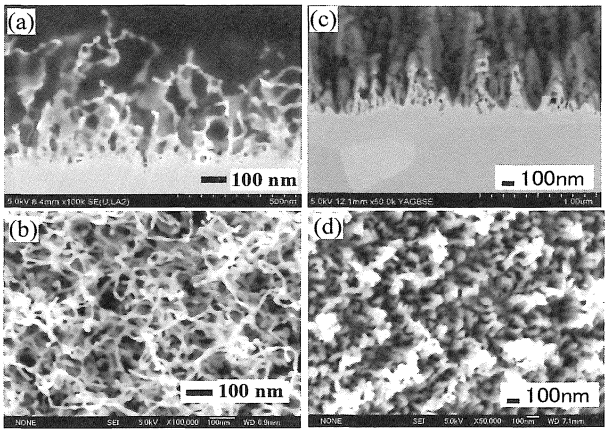

Figure 16. Comparison of tungsten surface morphology between original black surface with fiber-form nanostrucutre (a), (b) and those giving a sputtering minimum (c), (d), where (a) and (c) show the cross-sections, and (b) and (d) do the top surfaces.

5. Summary and conclusions

The effects of fiber-form nanostructure developed on tungsten surfaces on the particle emission form that surface are systematically represented for the first time. Generally speaking, the nanofiber-form forest made of tungsten with helium bubbles inside has a tendency of suppressing the particle emission.

We found that the electron emission comes not only from the impact of high energy primary electrons which makes the floating potential very deep compared with the value estimated by the bulk electron temperature, but also from the ion induced part which would be either Auger process and/or the ion impact SEE. At the moment it seems that the Auger process is dominating because that is no clear observation of ion energy dependence on electron emission.

The physical mechanism on the SEE suppression is discussed by using the Ohya's deep trough model, which is believed to be valid for both electron emission processes, SEE due to high energy electrons and ion induced electron emission.

The mechanism on the suppression of W physical sputtering is similar to that of electron emission suppression but is different from that since the sputtering changes the surface morphology. The thickness of original nano-fiber becomes fat on the way of proceeding the physical sputtering.

We discussed the suppression of physical sputtering in terms of the ratio of two surface area:

(1) the W surface area S_1 near the top surface facing to the incident heavy ions like Ar,

(2) the W surface areas S_2 which occupies deep troughs or valleys.

Of course, S_1 and S_2 are not well-defined values of surface area, but have a qualitative nature. When S_1/S_2 is small, then the sputtering yield would be small, while the sputtering yield approaches to that for flat W when its ratio becomes large up to 1.0.

In summary, we have to take into account the surface characteristics of tungsten in fusion reactor when one of the fusion products, helium may have a significant influence on the physical properties of plasma-facing component, and gives serious effect on reactor performance.

Acknowledgement

The research work was supported by Grant-in-Aid for Scientific Research (B) 20360414, Grant-in-Aid for Challenging Exploratory Research 23656578, and Grant-in-Aid for Scientific Research (A) 2246120 from JSPS, and also by the Science Research Promotion Fund from the Promotion and Mutual Aid Corporation for Private School of Japan. The authors would like to thank H. Iwata of Electrical Engineering in AIT for his help on FE-SEM manipulation.

References

[1] Takamura S., Ohno N., Nishijima D. and Kajita S. 2006 Plasma Fusion Res. **1** 051

[2] Baldwin M.J. and Doerner D.P. 2008 Nucl. Fusion **48** 035001

[3] Wright G.M., Brunner D., Baldwin M.J., Doerner R.P., Labombard B., Lipschultz B., Terry J.L. and Whyte D.G. 2012 Nucl. Fusion **52** 042003

[4] Kajita S., Takamura S., Ohno N., Nishijima D., Iwakiri H. and Yoshida N. 2007 Nucl. Fusion **47** 1358

[5] Kajita S., Takamura S. and Ohno N. 2009 Nucl. Fusion **49** 032002

[6] Tokitani M., Kajita S., Masuzaki S., Hirahata Y., Ohno N., Tanabe T. and LHD Experiment Group 2011 Nucl. Fusion **51** 102001

[7] Takamura S., Miyamoto T., Tomida T., Minagawa Y. and Ohno N. 2011 J. Nucl. Mater. **415** S100

[8] Takamura S., Miyamoto T. and Ohno N. 2010 Plasma Fusion Res. **5** 039

[9] Nishijima D., Doerner R.P., Baldwin M.J. and Yu J.H. 2011 J. Nucl. Mater. **415** S96

[10] Takamura S., Miyamoto T. and Ohno N. 2011 Proc. 38th EPS Conf. on Plasma Phys. O1-302, 27 June -01 July 2011, Strasbourg, France

[11] Kikuchi Y., Nishijima D., Nakatsuka M., Ando K., Higashi T., Ueno Y., Ishihara M., Shoda K., Nagata M., Kawai T., Ueda Y., Fukumoto N. and Doerner R.P. 2011 J. Nucl. Mater. **415** S55

[12] Masuzaki S., Ohno N. and Takamura S. 1995 J. Nucl. Mater. **223** 286

[13] Bergmann A. 2002 Nucl. Fusion **42** 1162

[14] Takamura S., Tsujikawa T., Tomida Y., Suzuki K., Minagawa T., Miyamoto T. and Ohno N. 2010 J. Plasma Fusion Res. SERIES **9** 441

[15] Imai K., Ohya K., Kawamura G. and Tomita Y. 2010 Contrib. Plasma Phys. **50** 458

[16] Kawata J. and Ohya K. 1994 J. Plasma Fusion Res. **70** 84

[17] Propst F.M. and Lüscher E. 1963 Phys. Rev. **132** 1037

[18] Hagstrum H.D. 1956 Phys. Rev **104** 309

[19] Mahadevan P., Layton J.K. and Medved D.B. 1963 Phys. Rev. **129** 79

[20] Kajita S., Yoshida N., Yoshihara R., Ohno N., Yokochi T., Tokitani M. and Takamura S. 2012 J. Nucl. Mater. **421** 22

[21] Miyamoto T. and Takamura S. "Recovery of Tungsten Surface with Fiber-form Nanostructure by the Effect of Surface Temperature Increase in Plasmas", accepted for publication in Plasma Sci. Technol.

[22] Beigman I., Pospieszczyk A., Sergienko G., Tolstikhina I.Yu. and Vainshtein L. 2007 Plasma Phys. Control. Fusion **49** 1833